Ultramicroscopy 148 (2015) 132–145

Contents lists available at ScienceDirect

Ultramicroscopy

journal homepage: www.elsevier.com/locate/ultramic

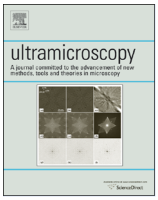

Electron imaging with an EBSD detector

Stuart I. Wright [a,*], Matthew M. Nowell [a], René de Kloe [b], Patrick Camus [c], Travis Rampton [c]

[a] EDAX, 392 East 12300 South, Suite H, Draper, UT 84020, USA
[b] EDAX, Ringbaan Noord 103, 5046 AA Tilburg, The Netherlands
[c] EDAX, 91 McKee Drive, Mahwah, NJ 07430, USA

ARTICLE INFO

Article history:
Received 16 June 2014
Received in revised form
9 October 2014
Accepted 13 October 2014
Available online 23 October 2014

Keywords:
EBSD
Synthetic-BSD
Virtual FSD
PRIAS
Electron imaging

ABSTRACT

Electron Backscatter Diffraction (EBSD) has proven to be a useful tool for characterizing the crystallographic orientation aspects of microstructures at length scales ranging from tens of nanometers to millimeters in the scanning electron microscope (SEM). With the advent of high-speed digital cameras for EBSD use, it has become practical to use the EBSD detector as an imaging device similar to a backscatter (or forward-scatter) detector. Using the EBSD detector in this manner enables images exhibiting topographic, atomic density and orientation contrast to be obtained at rates similar to slow scanning in the conventional SEM manner. The high-speed acquisition is achieved through extreme binning of the camera—enough to result in a 5 × 5 pixel pattern. At such high binning, the captured patterns are not suitable for indexing. However, no indexing is required for using the detector as an imaging device. Rather, a 5 × 5 array of images is formed by essentially using each pixel in the 5 × 5 pixel pattern as an individual scattered electron detector. The images can also be formed at traditional EBSD scanning rates by recording the image data during a scan or can also be formed through post-processing of patterns recorded at each point in the scan. Such images lend themselves to correlative analysis of image data with the usual orientation data provided by and with chemical data obtained simultaneously via X-Ray Energy Dispersive Spectroscopy (XEDS).

1. Introduction

Since the very first micrographs generated from data obtained using automated Electron Backscatter Diffraction (EBSD) or orientation imaging microscopy (OIM) [1], the appreciation of the ability of these maps to illuminate salient features of microstructure has steadily grown. Much of the early focus was on the quantitative crystallographic orientation data behind the images; but, the basic ability to form microstructural images from the OIM data has drawn many researchers unfamiliar with crystallographic orientation to EBSD. However, even with the speed of modern EBSD systems, the collection times required to obtain the orientation data precludes the use of OIM mapping as an imaging tool in the conventional sense.

One challenge for EBSD work is locating a suitable area on the sample for collecting EBSD data. As a highly tilted sample (~70°) with a smooth surface is preferred for producing good EBSD patterns, imaging the surface of the sample with traditional secondary electron imaging (SEI) or backscattered electron imaging (BEI) is difficult. To alleviate this challenge, EBSD detectors often have diodes mounted at various positions near the perimeter of the phosphor screen. These diodes capture electrons scattered in a forward direction due to the sample tilt and are thus generally termed forward-scatter detectors (FSDs). An FSD enables an operator to quickly collect a high-intensity and high-contrast image of the tilted sample surface. Thus, the sample can be surveyed using FSD imaging to locate a region for characterization via full EBSD analysis.

Day and Quested [2] showed the benefits of collecting multiple images of the same sample area using multiple diodes. They noted that these images differed from each other and proposed that they could be combined to create composite color images of the microstructure. While Day and Quested focused on the ability of these detectors to provide orientation contrast, others have shown that FSD imaging also shows atomic density (Z) contrast [3] and/or

---

Abbreviations: BEI, Backscatter Electron Image; BSD, Backscattered Electron Detector; CCD, Charge Couple Device; EBSD, Electron Backscatter Diffraction; FIB, Focused Ion Beam; IQ, Image quality as it pertains to the band-to-background contrast in an EBSD pattern; FPS, Frames per second; FSD, Forward-scattered Electron Detector; OIM, Orientation Imaging Microscopy; PRIAS, Pattern Region of Interest Analysis System; ROI, Region of Interest; SE, Secondary Electron; SED, Secondary Electron Detector; SEI, Secondary Electron Image; SEM, Scanning Electron Microscope; STEM, Scanning Transmission Electron Microscope; T-EBSD, Transmission Electron Backscatter Diffraction; TEM, Transmission Electron Microscope; TKD, Transmission Kikuchi Diffraction; VFSD, Virtual Forward-scattered electron Detector; WD, Working Distance; XEDS, X-Ray Energy Dispersive Spectroscopy

* Corresponding author: Tel.: +1801 495 2750; fax: +1801 495 2758.
E-mail address: stuart.wright@ametek.com (S.I. Wright).

http://dx.doi.org/10.1016/j.ultramic.2014.10.002

topographic contrast. The balance between the different contrast mechanisms changes depending on the position of the diode relative to the phosphor screen or more importantly relative to the point of incidence of the beam on the sample. For example the contrast differs when the detector unit is fully inserted compared to when it is retracted [4]. One of the drawbacks of using multiple FSDs is that each diode requires signal amplification in order to form an image. Thus, when multiple diodes are used either multiple amplifiers are needed or the images must be obtained sequentially through the same amplifier; thus, the benefits of multiple FSD detectors are often not fully realized.

As an extension of a study on image quality (IQ) mapping [5], Wright and Nowell explored using the EBSD camera itself as a set of multiple FSDs [6]. In essence, each pixel of the camera operates as an individual FSD. If the intensity at a specific pixel is recorded at each point during a scan then this data can be used to form an FSD-like image of the scan area. These initial studies [6] were performed using patterns recorded at each point during a scan using a typical camera operating condition (96 × 96 pixel patterns). The recorded patterns were further reduced in software to a 3 × 3 array of pixel bins. The intensities recorded within bins at each point in the scan grid were then used to form a set of individual microstructural images as shown in Fig. 1. As with multiple diodes, these images clearly showed differences arising from differences in the positions of the bins from which the images were formed.

The terms synthetic-BSD, virtual-FSD (VFSD), hybrid-FSD, and PRIAS (Pattern Region of Interest Analysis System) have all been used to describe the use of the EBSD detector as a set of multiple FSDs. Recently, there has been renewed interest in this type of imaging [7–9]. As in the Wright and Nowell [6] study, these studies have all been performed post-acquisition using patterns saved at each point of the scan grid during a conventional OIM scan. Indeed, this has given more impetus for saving of patterns during an OIM scan. One advantage of the CCD cameras used in modern EBSD systems is that they can be binned down in hardware to increase the collection efficiency of the EBSD detector and the speed of operation. Thus, instead of using an individual camera pixel as an FSD, a bin of pixels can serve as an FSD. This enables rapid imaging of the sample surface prior to performing EBSD analysis similar to FSD imaging.

2. Materials

The following materials are used in this study. They were selected so as to emphasize the effectiveness of the imaging technique to emphasize different elements of the microstructure. The working distance (WD) used for each sample is also listed.

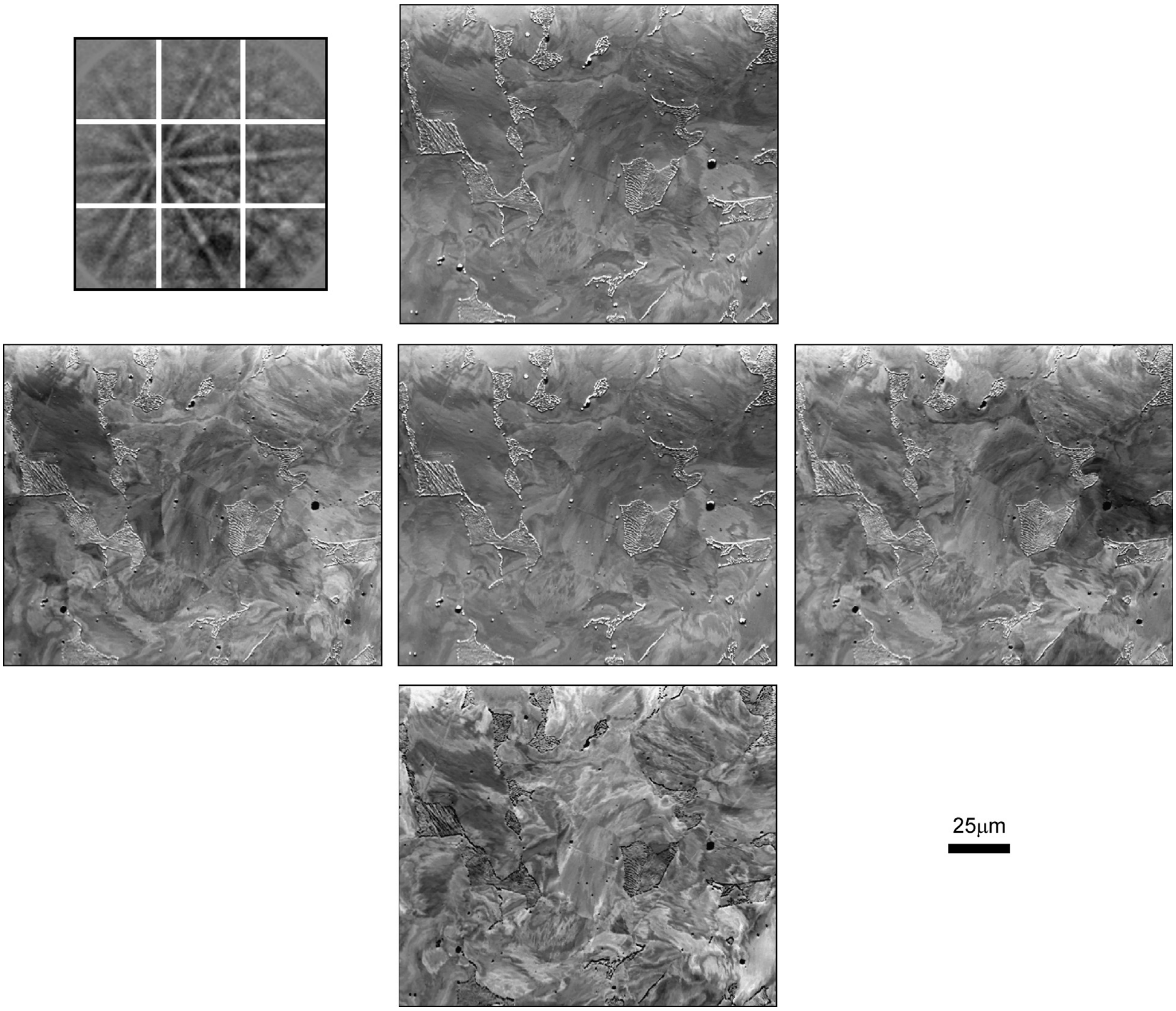

Fig. 1. VFSD images formed from five virtual apertures defined as squares on the EBSD pattern as shown in the inset.

- Ti–Al alloy—a multiphase sample containing alpha titanium, hexagonal Ti_3Al and tetragonal TiAl. 10.3 mm WD.
- Dual phase steel—a recrystallized 2205 ferrite-austenite steel that has been annealed to grow the Sigma phase. This sample was selected to investigate both orientation and phase contrast. 12.2 mm WD.
- Deformed steel—a deformed ferritic steel selected to investigate intergranular deformation contrast and had previously been used for FSD imaging studies—see Fig. 1. 11.9 mm WD.
- Molybdenum–Silicon—this sample contains three phases: $MoSi_2$, Mo_5Si_3 and Mo_3Si. 13.1 mm WD.
- Rhenium–Tungsten alloy—a solid solution alloy with a faceted surface. 14.8 mm WD.
- Zircon—this sample shows some metamictization due the presence of Uranium which causes the crystal to become amorphous. 15.9 mm WD.
- Nickel—this is an Inconel 600 EBSD reference sample, selected because it has orientation contrasts, topographic contrast from polishing, and some atomic number contrasts from both grain boundary and internal secondary intermetallic phases. This was imaged at different WDs as noted in the text.
- Copper foil—this sample exhibits a wavy surface. 13.8 mm WD.
- $AlTi_3$–$TiAl_3$ alloy—sample prepared for investigation by T-EBSD. 5 mm WD.

3. Mode

There are three modes for using the pattern pixel intensities to form microstructural images: (1) using highly binned patterns to simultaneously collect multiple FSD-like images enabling rapid imaging of the sample surface prior to performing EBSD analysis (pre-scan mode); (2) collecting and recording intensity data at fixed locations in the captured patterns concurrent with the usual orientation data during an OIM scan (concurrent mode) and (3) constructing images from EBSD patterns recorded during an OIM scan after the scan has completed (post-scan mode). Important details associated with each of these three modes are presented and discussed in the following sections.

3.1. Pre-scan mode

The objective of the pre-scan mode is to use the EBSD detector as an imaging detector in the same manner as a back-scatter, forward-scatter or secondary electron detector, either to select a suitable region-of-interest prior to collecting quantitative OIM mapping data for the OIM scan or to simply obtain high contrast microstructural images. This requires much faster acquisition of the individual patterns than those collected during a typical scan otherwise the acquisition time is simply too long to be practically considered an imaging technique.

3.1.1. Binning

The current cameras employed as EBSD detectors are CCD (charge-coupled device) cameras. One of the advantages of CCD cameras is the ability to combine the charges from adjacent pixels into a single readout signal. This process is called binning. For example, if a 640 × 480 pixel camera is binned down by a factor of 5, the resulting pixel dimensions of the image collected would be 128 × 96. This has two advantages from a speed point of view. The first is that the resulting image is smaller so that the data throughput from the camera into the computer is faster and any image processing is faster. However, a greater advantage is that a pixel in the binned image is essentially 25 times larger after 5 × 5 binning and is therefore a more effective light collector. This can have a dramatic impact on the exposure times needed to collect a pattern. Of course, the drawback of binning is reduced pixel resolution. However, for the EBSD mapping applications the full pixel resolution provides only marginal benefit for the orientation measurements [10].

As noted in the introduction a separate microstructural image can be formed for each pixel in the EBSD pattern. However, too many images become cumbersome. We have settled on an array of 5 × 5 images as a tractable number. It provides a small enough number of regions of interest (ROIs) to show orientation contrast and flexibility for making composite images by combining different images together (these topics will be discussed in detail in subsequent sections) and not so many as to make manipulating the images unnecessarily complex. Thus, the final pattern is only a 5 × 5 pixel image as shown schematically in Fig. 2. The notation used in this figure will be used in the remainder of the paper to denote the individual VFSD images. It should also be noted in this figure that while the CCD array actually is rectangular we have cropped off the left and right edges to form a square in which the circular phosphor screen is inscribed. It should be noted that the corner bins in this square are not fully covered by the phosphor screen. This results in lower signal levels in these bins; nonetheless, good images are generally formed in these regions albeit with lower signal-to-noise ratios.

We have found that binning the camera down by a factor of 10 to a 48 × 48 pixel pattern produces very good results. Higher speeds can be achieved by binning the camera down to as small as 15 × 15 pixels, with slight increases in image noise. The remaining binning down to a 5 × 5 pixel pattern is done in software. Fig. 3 shows 256 × 200 pixel images collected from the Ti–Al sample at two binning levels—the high binning level image was collected in 24 s and the low binning level in 68 s. It is clear from these results that the noise increases at higher binning levels. However, the increased noise is not inherent to the binning process; rather, it is simply due to the increased speed of collection—i.e. shorter dwell times. Averaging multiple frames for each pattern decreases this noise but at the cost of slowing the image acquisition speed.

With the binning described here, 25 VFSD images can be collected simultaneously at rates similar to conventional slow-scan imaging on the SEM. A 256 × 200 pixel image requires 29 s using the 48 × 48 binning level using an EDAX Hikari Super camera and a 1024 × 800 pixel images commensurately requires nearly seven minutes. The frame rate at this level of binning was over 2000 frames per second (FPS). The ability of modern EBSD systems to operate at these higher frames is critical in using the EBSD camera as an imaging detector in the pre-scan mode. For a camera that can operate at only 100 FPS, the time needed to collect at 1024 × 800 pixel image would take over 2 h; thus, slower cameras are unsuitable for operation as pre-scan imaging detectors but they are still suitable for obtaining VFSD in the concurrent and post-processing modes. At these high-speeds it is also important that the phosphor screen have a decay time short enough to prevent any persistence of the previous pattern as the

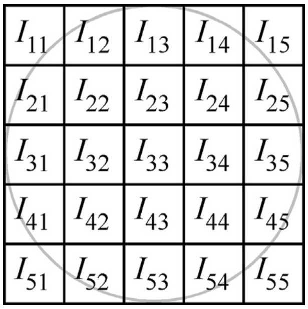

Fig. 2. Schematic of bin locations for a 5 × 5 pixel pattern.

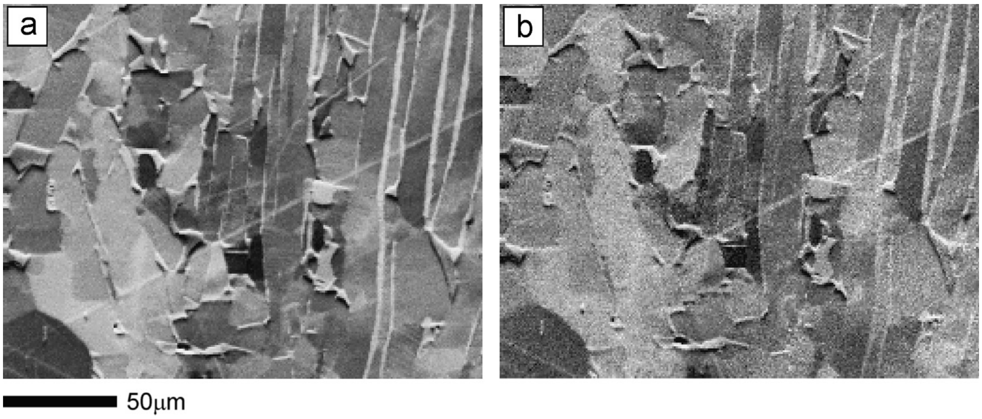

Fig. 3. I_{53} images collected from the TiAl sample in pre-scan mode in a (a) low binning (48 × 48 pixel patterns)/low speed (758FPS) configuration and (b) high binning (15 × 15 pixel patterns)/high speed (2207 FPS) configuration.

beam moves from pixel to pixel in the scan grid. For the system used here, a phosphor with decay to 10% in 37 µs was used.

It should be noted that 5 × 5 pixel patterns cannot be indexed to determine the crystallographic orientation from these patterns and no attempt is made to do so. Rather, the intensities at the individual pixels in these highly binned patterns are used solely for imaging. It should also be noted that the time required for any post-processing increases as the resolution increases. However, the computation time for post-processing (see Sections 4.1 and 5.1) is negligible with the exception of the pattern difference calculations (see Section 5.2).

3.1.2. Comparison to traditional SEM based imaging

The main difference between VFSD imaging and conventional SEM imaging lies in the source volume and especially the electron trajectories. SE images are generated from low energy electrons, typically below 50 eV, originating from the top few nanometers of the sample surface. The contrast is usually topographic in origin and is due to the efficiency of SE electron generation as function of surface tilt and the path that these electrons have to travel around obstacles. On the vast majority of EBSD samples, this SE contrast is low because typical samples have highly polished surfaces. In backscattered electron imaging with a horizontal sample, the majority of the signal comes from the higher energy electrons from within a larger source volume when compared to SEI. These electrons are scattered back towards the BSE detector mounted close to the SEM lens. When the sample is tilted most electrons area scattered downwards in the direction of the EBSD detector and the BSE signal weakens significantly.

An FSD system usually consists of one or more BSE diodes mounted around the perimeter of the EBSD phosphor screen. The locations of these detectors are selected to optimize the electron intensity for the typical EBSD sample geometry considering the limitation that the screen itself is in the optimum position for the highest electron intensity. Thus, in order to optimize the FSD signal on any given diode requires placing the EBSD detection system in a geometry that is not as ideal for general EBSD use. Generally, a diode positioned below the phosphor screen provides the best FSD image for an EBSD detector in the normal operating geometry as it provides the best signal without masking the phosphor screen. In addition, the total signal for any given diode depends on the collection area of the diode being used. The smaller the diode/ROI the higher the expected FSD sensitivity to orientation changes. Larger diodes or the capture of a larger ROI of the EBSD pattern also means an increased sampling of the background intensity cone. Thereby, larger diodes/ROIs are more sensitive to atomic number and topographic effects and less to orientation changes.

For any electron detector, the acquisition speed depends on the selected pixel dwell time needed to provide the desired signal-to-noise ratio in the image. This typically ranges from few µs for SE to several 10's of µs for BSE images. Hardware FSD diodes have comparable intensity and quality as BSEs and require similar acquisition times. The obtainable speed of the virtual FSD is limited by the EBSD camera acquisition speed which currently corresponds to a minimum dwell time of ~450 µs.

Thus, using the phosphor screen itself as a VFSD with flexible bin size selection has a size advantage over the smaller individual FSD diodes. Deriving the diffraction signal from the phosphor screen has all of the geometric benefits of hardware diodes and provides detection in the high intensity regions. One disadvantage of the VFSD is that the efficiency of hardware diodes is higher than the phosphor screen-camera detection arrangement.

3.2. Concurrent mode

Various parameters are saved during an OIM scan—orientation data, pattern quality metrics, indexing reliability as well as X-Ray counts during simultaneous EBSD/XEDS scans. These data can be used in a wide variety of ways to make gray and color scale maps to examine many different aspects of the microstructure. Since a pattern is captured at every point in the scan grid it is also possible to record the intensities at various ROIs on the pattern. In the current implementation we have elected to store the average intensities at three different ROIs. These scalar values are recorded at each point in the scan and can be mapped and analyzed in the same way as the IQ value recorded at each point [5]. There is no discernible impact on the speed of data acquisition in recording these three values. The only drawback is the additional memory required to load these additional values into the post-processing software and additional disk space required to store the values. The currently selected ROIs for this analysis are a strip at the top, a strip at the bottom and a square located at the center of the pattern as shown in Fig. 4. The data for the top and bottom strips are obtained from the raw EBSD (camera) pattern whereas the data from centered square is obtained from the EBSD pattern after any operator-defined image processing is applied to the incoming pattern. At a typical EBSD WD of approximately 10–15 mm, the top strip is more sensitive to topographic and atomic density contrast whereas the other two ROIs are more sensitive to purely crystallographic orientation. The various competing contrast mechanisms will be discussed in more detail in subsequent sections.

Of course, more ROIs could be defined and intensities recorded but we have selected only three at this time. If more ROI data is needed then this can be achieved by saving the patterns at each point in the scan. The analysis of recorded patterns is described in the following section.

3.3. Post-scan mode

For ultimate flexibility in the images that can be formed from the patterns, the patterns at each point in an OIM scan can be recorded. The penalties for recording all the patterns are those associated with big data—disk space, computer memory, speed of recording patterns, and speed of loading of patterns into the post-processing software. However, these drawbacks are offset by the power and flexibility of having the full pattern available for analysis.

Since the camera image is stored at each point in the scan, the number, size, and shape of the virtual apertures can be defined as deemed useful. Images from any aperture can then be formed and mixed with images from other apertures to create an infinite variety of composite images.

The patterns are saved at the camera resolution specified by the operator when setting up the OIM scan. If the same aperture definitions are used for the post-scan mode as in the pre-scan mode then the number of camera pixels in the saved patterns will typically be much higher in the post-scan mode. In addition, there is no requirement that the number of scanned pixels in the pre-scan images matches the number in the OIM scans. Thus, there will be subtle differences in the pre- and post-scan images. An example is shown in Fig. 5 for the I_{53} image for a scan on duplex steel. In this example the pre-scan image has dimensions of 512 × 400 pixels collected in a square grid, the OIM scan has 180 × 140 pixels in a hexagonal grid, and the patterns recorded in the OIM scan had dimensions of 96 × 96 pixels.

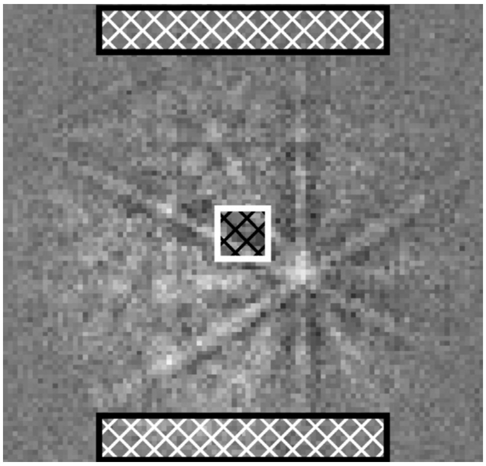

Fig. 4. Location of ROIs overlaid on pattern for the concurrent mode.

In the current implementation, each pattern is recorded both before and after any image processing has been applied to the pattern prior to indexing the pattern. This allows for more flexibility in generating images using specific scattering or diffraction contrast mechanisms from the pattern data.

4. Image contrast

As the intensities from which these images are generated are obtained directly from diffraction patterns, the images tend to show contrast based on individual scattering and/or diffraction/channeling events at each pixel in the image. These events primarily elucidate three types of physical attributes of the sample: topography, atomic density (or Z) and crystallographic orientation. In most cases, we have observed that topographic contrast is generally the most dominant, followed by atomic density and then by orientation. Fig. 6 shows an example of three different samples in which these different contrast mechanisms are clearly evident. While these images show clear evidence for topographic, phase and orientation contrast; often the contrast is more subtle and difficult to differentiate. The balance between the different contrast mechanisms is due, in part, to geometrical differences.

4.1. Geometry effects

The intensity that arrives at the EBSD phosphor screen depends on all of the contributions to the electron emission from the interaction volume of the electron beam on the sample. In the EBSD geometry, the basic intensity variation is the vertical and lateral intensity changes associated with the x–y scanning of the image. The positional variation on the scan directly modifies the positional change on the screen. At high magnifications, the positional variation is small. However, at low magnifications the vertical shift and to a lesser extent the lateral shift can introduce intensity variations that are not related to the sample structure but simply vary due to geometry as shown schematically in Fig. 7 and experimentally in Fig. 9. These geometric effects occur with both hardware and virtual detectors.

In general, ROIs at the bottom of the phosphor screen tend to be more sensitive to topography as the electron path vectors become closer to parallel with the sample surface, especially at shorter WDs as shown by the dashed vector in Fig. 7(b). For the images shown in this paper the camera is tilted at an angle of 10° below the horizontal. The perpendicular distance from the center of the phosphor screen to the beam line is 17.2 mm and intersects

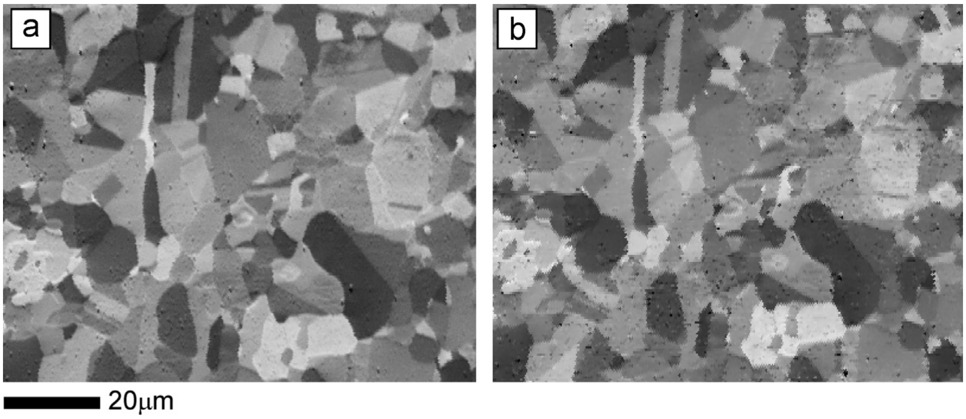

Fig. 5. I_{53} images of the same region of a dual phase steel sample collected (a) in pre-scan mode over a mapping area of 512 × 400 pixels and (b) in post-scan mode over a mapping area of 180 × 140 pixels.

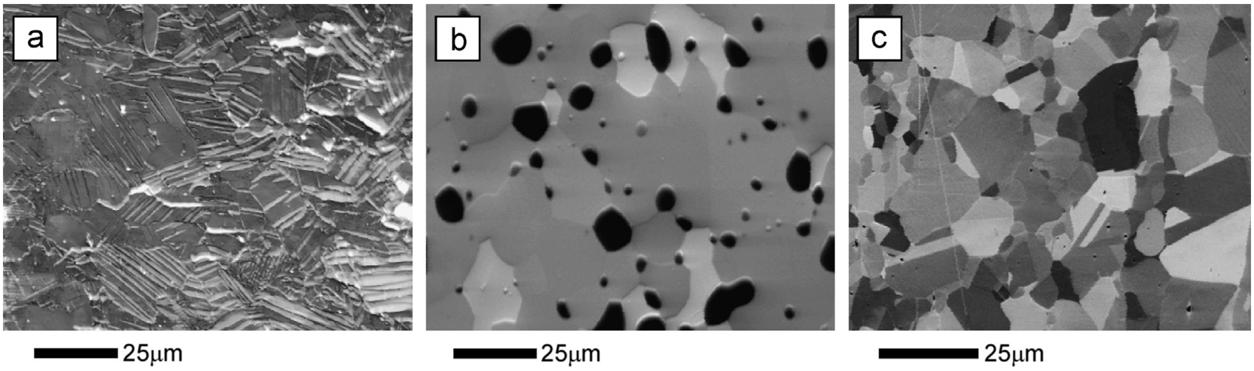

Fig. 6. Sample VFSD images from (a) a Re–W sample showing topographic contrast, (b) a Mo–Si sample showing atomic number contrast and (c) a recrystallized dual phase steel sample showing diffraction contrast.

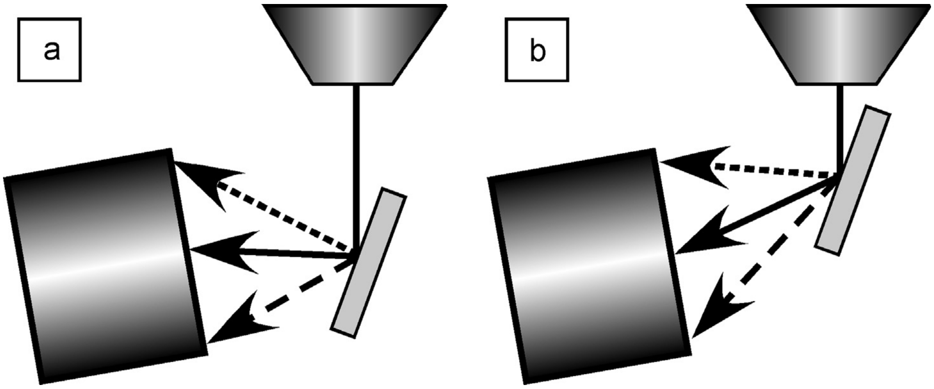

Fig. 7. Schematic of the impact of the WD on the geometrical effects in VFSD images.

the beam line at a WD of 21.2 mm. This geometry is slightly different for the copper foil sample but only varies within ± 2 mm.

At a short WD, a given pole will intercept a certain binned pixel. If the WD is increased by 10 mm then the location of that same pole will drop by 10 mm on the screen. If this new location moves to another binned location, it is easy to envision a change in contrast solely due to the acquisition geometry. This can be observed in Fig. 8 showing the same VFSD image from the same sample at two different WDs. Although it is not obvious at the resolution displayed, the image at 23.1 mm is noisier than the image at 9.6 mm indicating less efficient signal collection at this WD for the geometry of the collection system (optimized for a 10 mm WD). This is equivalent to obtaining VFSD images from different ROI's on the EBSD detector with a stationary sample. It illustrates the flexibility of the VFSD imaging method to position a virtual diode at the optimum position for desired image contrast.

Some aspects of the geometric variations can be reduced if background removal techniques are used on the collected diffraction patterns prior to forming the VFSD images. This is evident in Fig. 9. In addition, some image processing can improve the images as well. We have found that using intensity normalization on each image individually greatly enhances the contrast of the images, while normalizing the intensities across all the images together does not provide near as much improvement. The majority of images displayed in this paper have undergone such normalization.

4.2. *Topographic contrast*

Most samples prepared for EBSD are polished and thus have a very smooth surface, especially if these are primarily single phase samples. Multi-phase samples may exhibit more surface topography due to differential polishing rates during preparation. Some samples are not metallographically prepared prior to investigation by EBSD but are investigated in the as-processed condition such thin-films and in-situ tensile samples. These samples are not smooth but can have significant surface topology. The varying surface can markedly affect the intensity at each location in the VFSD. It should be noted that the VFSD is sensitive to both topographic (sharp discontinuous surface structures such as facet, pores and cracks) and topological features (smooth continuous surface features such as wavy surfaces); however, we have elected to clump these two terms together and use the term topography to describe the contrast related to surface features. The ability of VFSD to provide topological information is evident in Fig. 10 which is from a copper foil. The SEI shows both topological and topographic contrast but the I_{31} VFSD image from this sample shows the topological wavy nature of the sample much more prominently.

The geometric effects are clearly evident on a sample with a faceted topography as shown in Fig. 11. Fig. 11 shows an image from the left side and an image from the right side of the 5 × 5 array: I_{31} and I_{35}. It is clear that the geometry affects the “shadowing” of topographic samples as there is a left-to-right reversal of intensity at the edges of the facets in the two images. Generally, there is also a switch in the shadowing from top to bottom between I_{15} and I_{53} although this depends on the WD. Topography effects in SE images are not shadowing in the same sense as in VFSD images. The VFSD shadowing is a direct blocking of the line of sight while SEI electrons can travel “around the corner” towards the SE detector. VFSD shows strongest topographic contrast for electrons traveling close to parallel to the sample surface as that amplifies any shadowing due to surface irregularities.

4.3. *Z-contrast*

Fig. 12(a) displays an image from zircon showing strong *z*-contrast. This image is shown alongside a blended color map constructed from

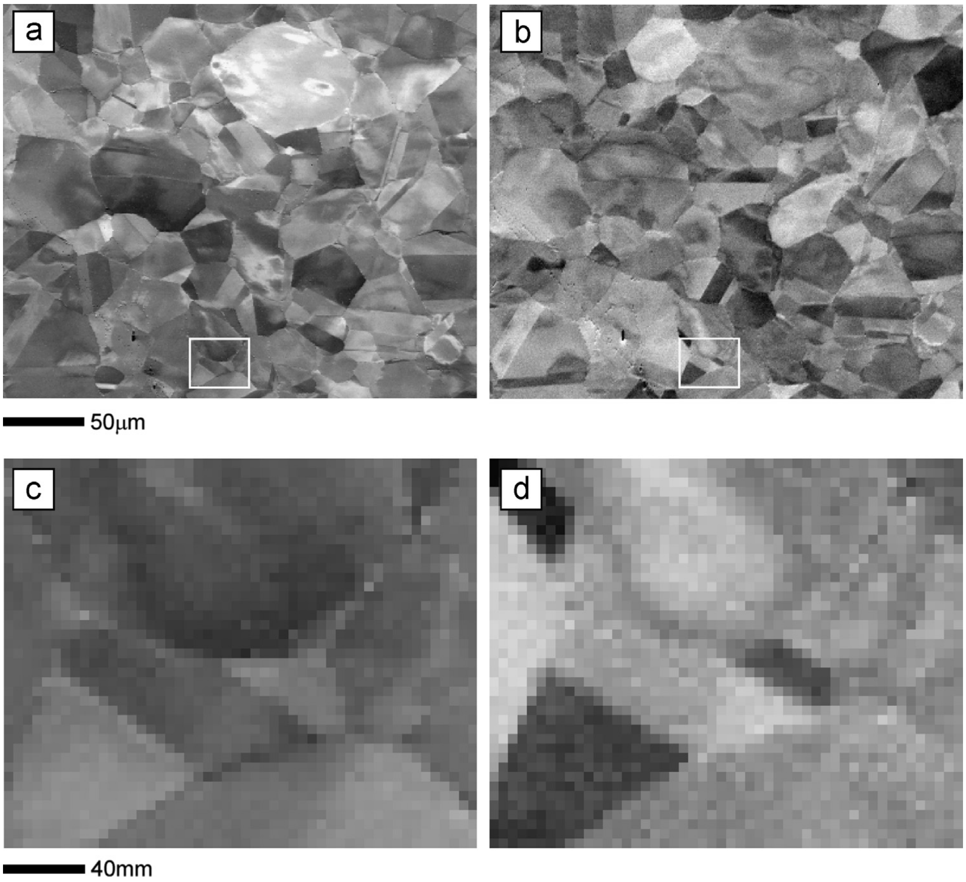

Fig. 8. I_{33} images from a nickel sample (no pattern processing) at a WD of (a) 9.6 mm and (b) 23.1 mm. (c) and (d) are magnified versions of the outlined regions (800 ×) in (a) and (b) respectively.

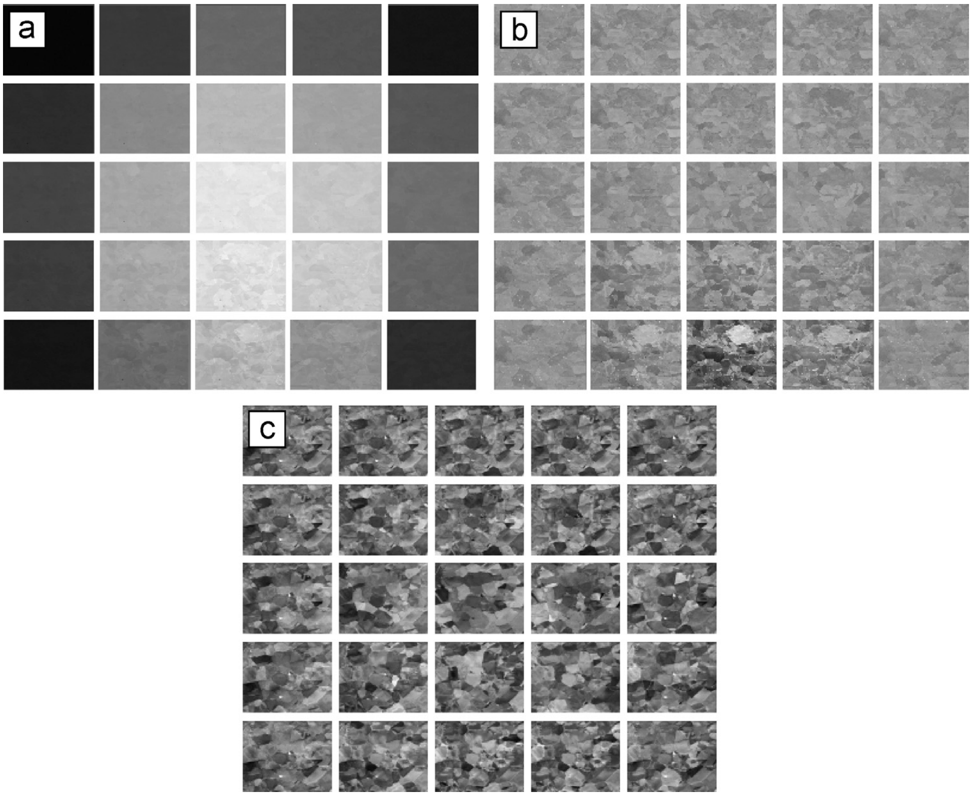

Fig. 9. Full series of images on the nickel sample at a 9.6 mm WD in pre-scan mode without any image processing (a) without and (b) with with static background correction of the EBSD patterns. (c) The same series of images as in (b) after intensity normalization of each image individually.

simultaneously collected XEDS data for comparison as well as a BEI and an IQ map. There is clearly a correlation between all these images. It should be noted that we show only one of the 25 VFSD images. This single VFSD image does not show all the features observable in the other images; however, most of these features are visible in at least one of the other 24 VFSD images including the area of metamictization at the center of the zircon grain.

It should be noted that the interaction volume associated with EBSD is typically an order of magnitude smaller than for XEDS. Thus the *z*-contrast achievable with VFSD provides the advantage of linking elemental information with crystallographic orientation information at the same spatial scale. This could provide an enhancement over the phase differentiation process using simultaneous EBSD/XEDS on some samples [7,11].

4.4. Orientation contrast

Fig. 13 shows the I_{52}, I_{53}, and I_{54} images for a fully recrystallized dual phase steel polished to a very smooth surface. Although the material contains 2 phases, the composition differences are not very large and the diffraction or orientation contrast dominates. Since the material is crystalline, the image is showing strong crystal orientation contrast. A quick visual inspection of these images shows that grains switch from light to dark from one image to another. Based on the typical EBSD geometry where the phosphor is positioned approximately 20 mm from the sample, the left and right images are constructed from electrons arriving at the detector at approximately $\pm 14^\circ$ degrees from the center image.

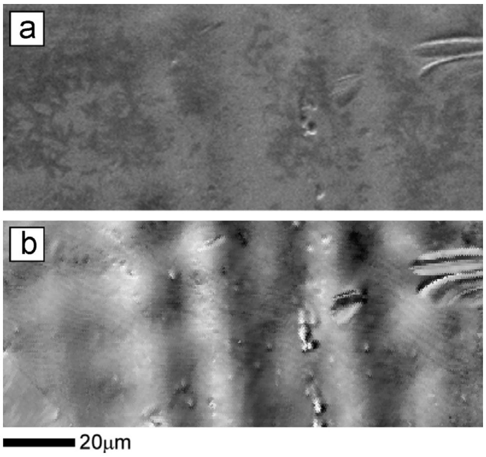

Fig. 10. (a) SEI of the copper foil sample and (b) I_{31} post-scan VFSD image from a copper foil sample.

Light grains are generally denoted by a strong pole or zone axis being positioned in the bin from which the image was constructed. Dark grains arise due to a lack of any high intensity features in the selected bin of the corresponding pattern. This effect is illustrated in Fig. 14. It should be noted that while 96 × 96 pixel patterns are shown in the figure the actual images were formed from the 5 × 5 pixel patterns. Each of these bins of pixels can be thought of as an aperture capturing the intensity in that diffraction direction analogous to the process of dark-field imaging in the TEM.

This is all quite easy to interpret in a fully recrystallized material. However, in a deformed material, the very small rotations that occur within the grain interiors produce large changes in local intensity in these images. This is clearly evident in the I_{33} image shown in Fig. 15 for the deformed steel sample. These large localized changes in image contrast are caused by small rotations which move a specific high intensity pole or band in-to or out-of the specified imaging ROI. Reducing the size of an imaging ROI tends to enhance this contrast.

4.5. Mixed contrast

Fig. 16 shows images from the molybdenum–silicon sample where *z*-contrast, topographic and orientation contrast are all evident in single sample and can be differentiated from each other. Fig. 16(a) shows an image from the top row, I_{13}, which is dominated by *z*-contrast. The three phases in this sample are clearly delineated. The image from the center of the bottom row of virtual FSDs, I_{53}, shows both orientation and topographic contrasts. The orientation contrast within the phases is evident for both the mid-level intensity phase as well as the bright phase as highlighted by the arrows in Fig. 16(b). The choice of WD in this case is fortuitous in that the I_{13} image is almost free of any shadowing characteristic of topography; whereas it is clearly evident in the I_{53} image.

5. Image construction

5.1. Composite imaging

Having an array of images from the use of multiple ROIs allows an operator to mix the different signals together to form composite images in order to try and isolate, enhance, or suppress a given contrast.

This can be done in a variety of ways. The user can sum several images together in order to reduce noise. Note, however, that summing images blur the bin-to-bin variations discussed in Section 3.1.1. It may also be useful in some case to subtract one

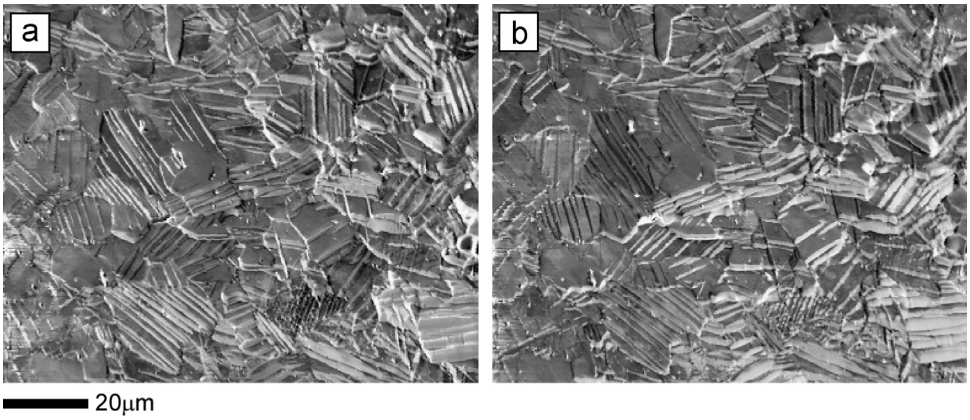

Fig. 11. I_{31} and I_{35} pre-scan images of Re–W sample.

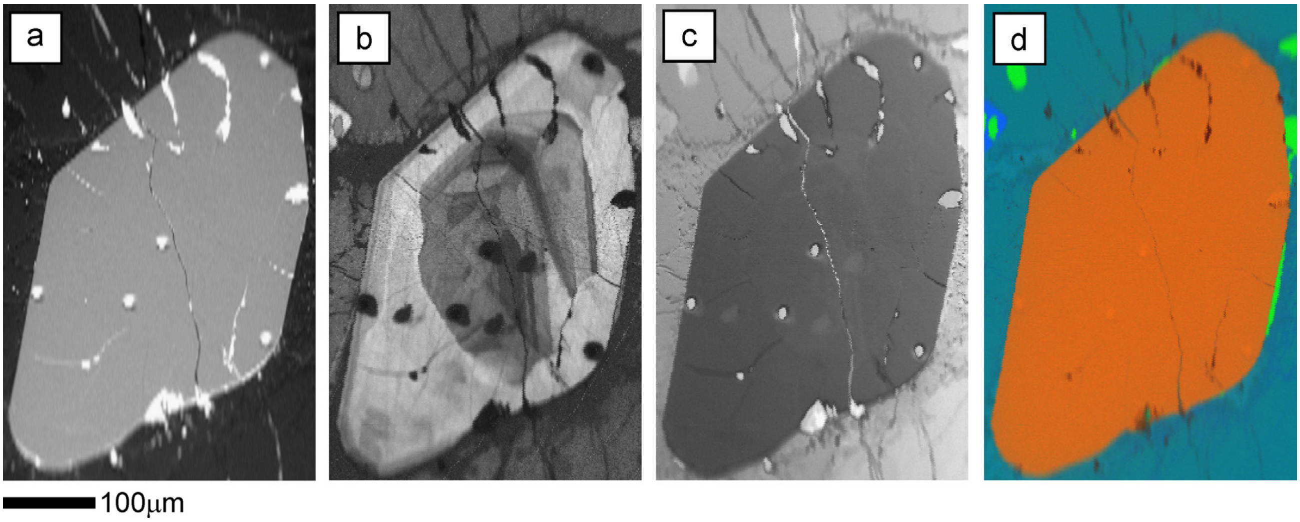

Fig. 12. (a) Backscatter electron image, (b) IQ map, (c) I_{53} post-scan image and (c) blended elemental map (Zr—Red, Si—Green, Al—Blue) of a zircon sample. (For interpretation of the references to color in this figure legend, the reader is referred to the web version of this article.)

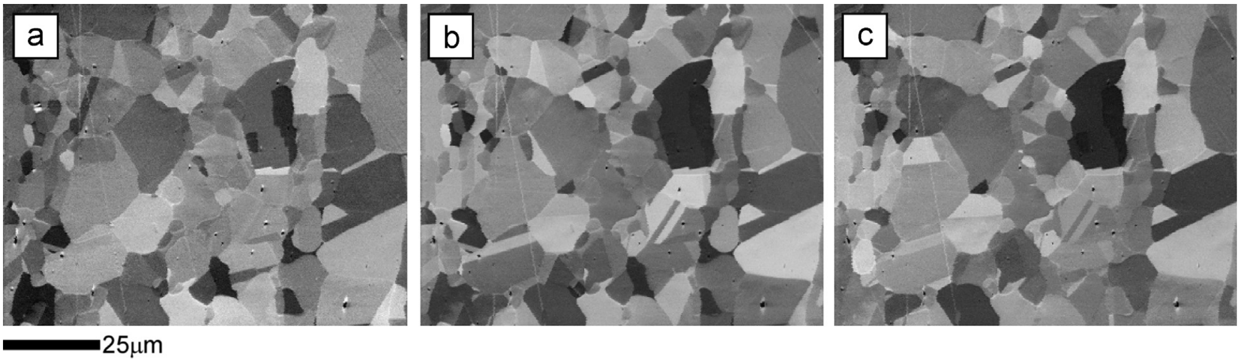

Fig. 13. (a) I_{52}, (b) I_{53}, and (c) I_{54} images generated from patterns from dual-phase steel in post-scan mode.

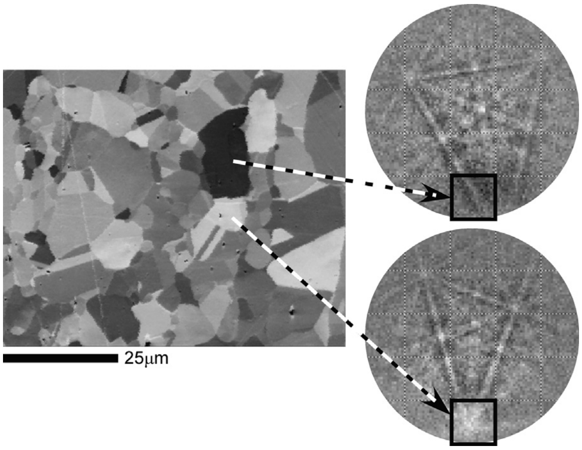

Fig. 14. Comparison of the pixel intensities for two grains in an I_{53} image from a dual-phase steel with corresponding patterns showing different pole intensities within the I_{53} imaging aperture.

image from another to highlight small differences between two images.

As Day and Quested [2] showed, the different images can be combined together to create composite color and gray scale images to highlight features of interest. For example, Fig. 17 shows a composite color image created by setting the I_{42} image to the red component of the color image, the I_{43} to green and the I_{44} to blue. The orientation contrast is much more evident in the pseudo-color image relative to the individual images which focus the attention on the topographic contrast.

On a fully recrystallized material these pseudo-colored images can be quite useful to delineate the individual grains in the images as shown in Fig. 18 which shows a composite VFSD image in (a) and the corresponding orientation map generated from the EBSD data collected over the same area in the conventional manner in (b). It should be emphasized that the colors in Fig. 18(a) are simply due to a red–green–blue assignment to three gray scale images and provide no quantitative information on the crystallographic orientation whereas in map shown in (b) the colors are generated from the underlying quantitative EBSD data have distinct meaning relative to the crystallographic orientation.

It should also be emphasized that we have only begun experimenting with identifying the best set of contributing VFSD images to a composite color image. We have found that the sample itself as well as the SEM and EBSD imaging conditions and the geometrical relationship between the pole piece, sample and EBSD detector all have an impact on the contrast in the VFSD images. Thus, a generic recipe for suppressing, enhancing or isolating the different contrast mechanisms is not yet within reach. As a guideline, we have found that smaller ROIs tend to lead to stronger orientation contrast.

5.2. Pattern difference map

As mentioned in Section 5.1, it is possible to highlight differences in images by subtracting one image from another. Another way to highlight the differences is to construct a pattern difference map.

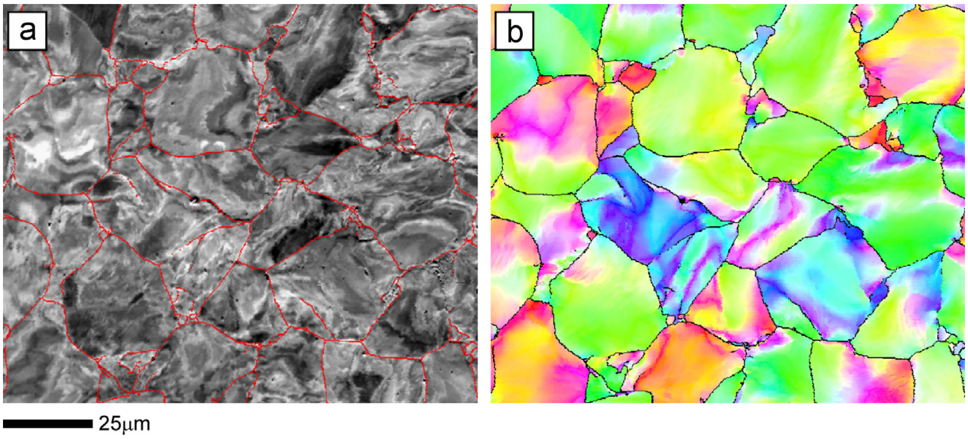

Fig. 15. (a) VFSD centered-square map in concurrent mode and (b) IPF map from deformed steel both overlaid with $>15^\circ$ boundaries.

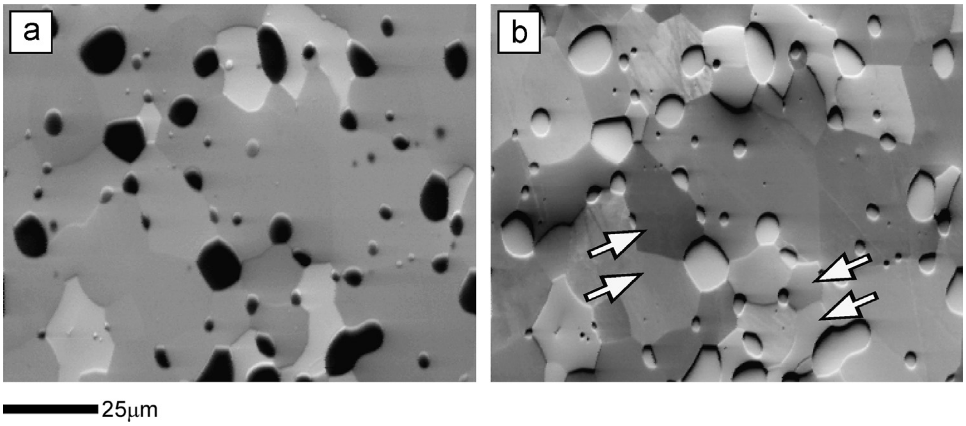

Fig. 16. (a) I_{13}, and (b) I_{53} pre-scan images of Mo–Si sample.

This image is generated by comparing the pattern at each point with the patterns of the neighboring points. Fig. 19(a) shows an example of a pattern difference map for the recrystallized dual phase steel. The pattern difference is calculated following the method proposed by De Graef [9]. In this method, each pattern is converted into a column vector. The intensity at each pixel in the pattern becomes a component of a vector. The average intensity of the pattern is then subtracted from each vector component and the vector is normalized. The difference between two patterns is determined by calculating the dot product between the two normalized pattern vectors. In the implementation presented here, the absolute value of the dot product is used so as to focus on the difference between the two patterns. The range for the calculated value is 0 to 1; however, this value is subtracted from 1 so that a value of 0 indicates no difference between two patterns and 1 represents the maximum difference. For each pixel in the map, the difference between the pattern associated with the pixel and the patterns of the neighboring pixels is calculated. The maximum value of the difference calculations is then assigned to the pixel and mapped to a gray scale (or color scale) to form a pattern difference map as shown in Fig. 19(a). This is similar to the Kernel Average Misorientation map [12] but instead of the average misorientation in the kernel being calculated and mapped the maximum misorientation in the kernel is used in the pattern difference map. Fig. 19(b) shows a kernel maximum misorientation map calculated in this manner for comparison. In this deformed material, it is clear that the pattern difference metric is very sensitive to low angle misorientations.

Fig. 20(a) and (b) shows a range of intensities at the boundaries indicating greater pattern difference. Some boundaries do not appear very bright but are evident due to differences within the grains themselves—these are highlighted by the arrows in Fig. 20. This is unexpected as patterns should be essentially identical within the grains in this fully recrystallized material; however, it has been found that image processing applied to the incoming patterns can either increase or diminish this effect—in this case a static background subtraction procedure was used. Using dynamic background subtraction [13] tends to reduce the internal grain-to-grain variation in intensity. The orientation spread within the grains was calculated and found to be small as expected and also showed no correlation with the in-grain intensities in the pattern difference map. No correlation was found between the IQ and the pattern difference values for the points in the grain interiors either. At this juncture, the variance in the in-grain pattern differences is unclear. It should also be noted that the twin boundaries tend to be much less decorated than the other boundaries (see the highlighting arrows in Fig. 20 (a) and (b). This suggests, that the intensities within some of the bins are very similar which make sense as the patterns at either side of twin boundaries tend to have a strong pole in the same position within the pattern and share some of the same band locations as well. Fig. 20(c) containing a kernel maximum misorientation map is included for reference. The maps in (a) and (c) are maps from OIM data on a 375 × 300 point hexagonal grid and (b) is a 512 × 400 pixel map.

In the samples we have investigated we have observed that while the boundaries correlate well with the pattern difference map in terms of their position, they do not correlate in terms of magnitude. There is little or no correlation in the pattern difference metric and the misorientation angle.

Maps constructed from the pattern quality parameter(s) recorded during OIM scan are commonly used to visualize various aspects of

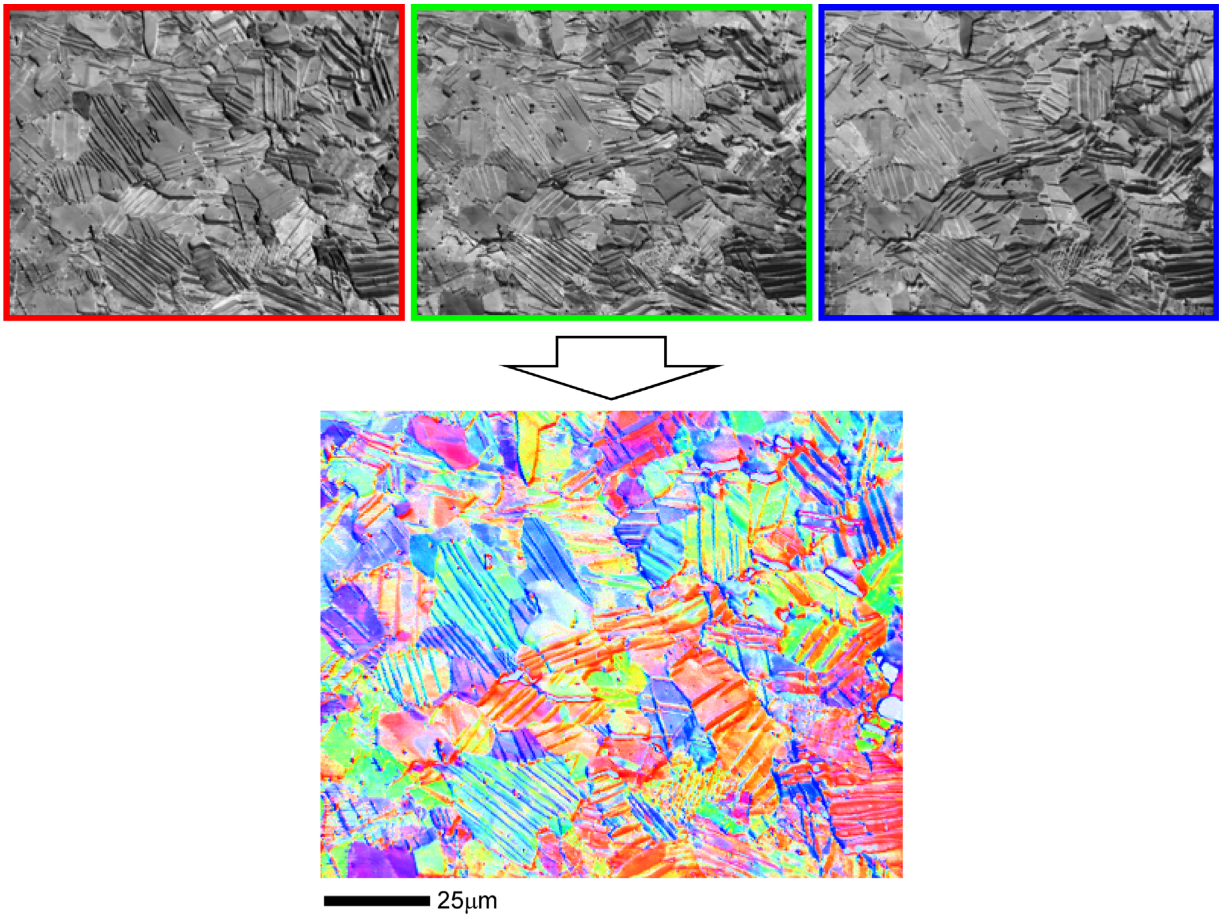

Fig. 17. Flow chart for constructing a composite color image through the assignment of red, green, and blue to the I_{42}, I_{43} and I_{44} VFSD images for the Re–W sample. (For interpretation of the references to color in this figure legend, the reader is referred to the web version of this article.)

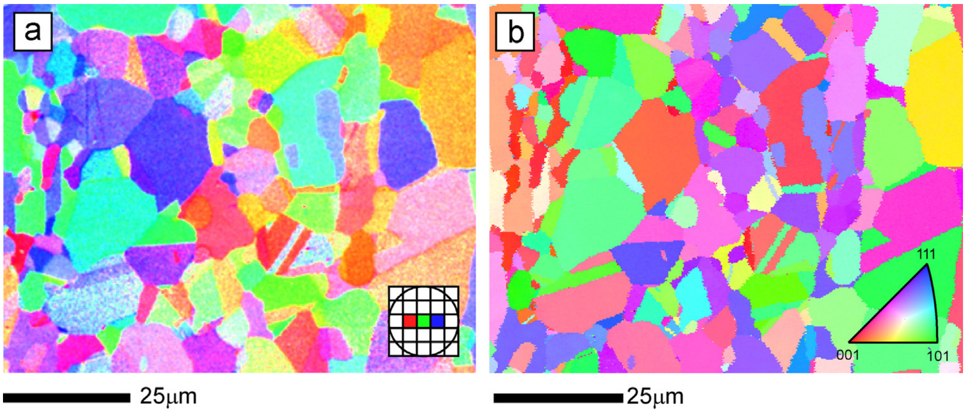

Fig. 18. (a) Composite VFSD image of a recrystallized dual phase steel accompanied by a schematic of the color channel assignment and (b) an orientation map for the same sample accompanied by a unit triangle showing the orientation coloring scheme. (For interpretation of the references to color in this figure legend, the reader is referred to the web version of this article.)

the microstructure [5]. VFSD images do not provide as much information on the quality of the EBSD patterns as an IQ map; which is the band-to-background contrast. This is evident in Fig. 21. The dark needle-like structures are not as prominent in the VFSD image as in the IQ map. In this example, the patterns from the dark and bright “blobs” exhibit less band-to-background contrast than at surrounding points in the microstructure even though they are at the same orientation. However, this noisier pattern is very well reflected in the pattern difference map as is evident when comparing Fig. 21(b) and (c) albeit with reversed intensity. The reason behind the diminished IQ is under investigation.

6. Transmission EBSD

Trimby [14] has shown the value of FSD imaging in Transmission EBSD (T-EBSD) also referred to as Transmission Kikuchi Diffraction (TKD) [15–17]. Like with solid state FSD detectors, VFSD imaging

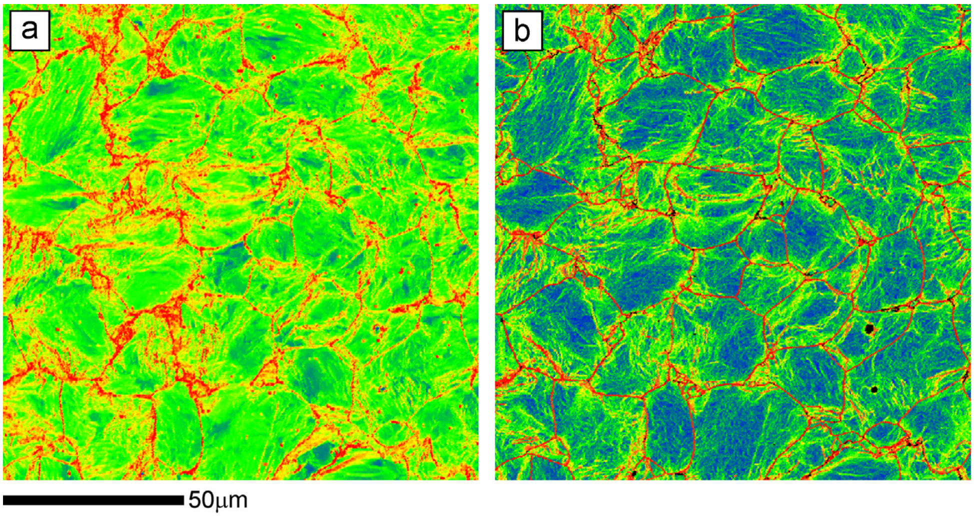

Fig. 19. (a) Pattern difference map and (b) kernel maximum misorientation map from the same area for a deformed bcc sample as shown in Fig. 15. (For interpretation of the references to color in this figure legend, the reader is referred to the web version of this article.)

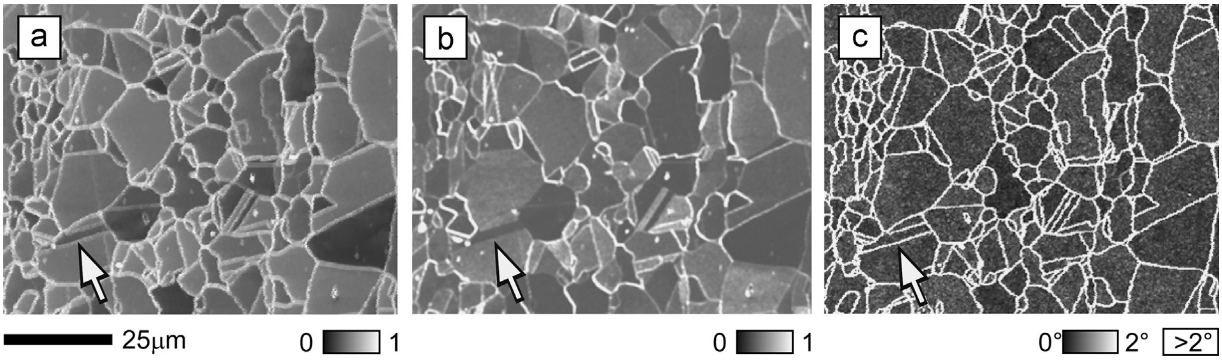

Fig. 20. (a) A pattern difference map constructed from 96 × 96 pixel patterns recorded during the OIM scan, (b) a pattern difference map from data obtained in pre-scan mode and (c) a kernel maximum misorientation map.

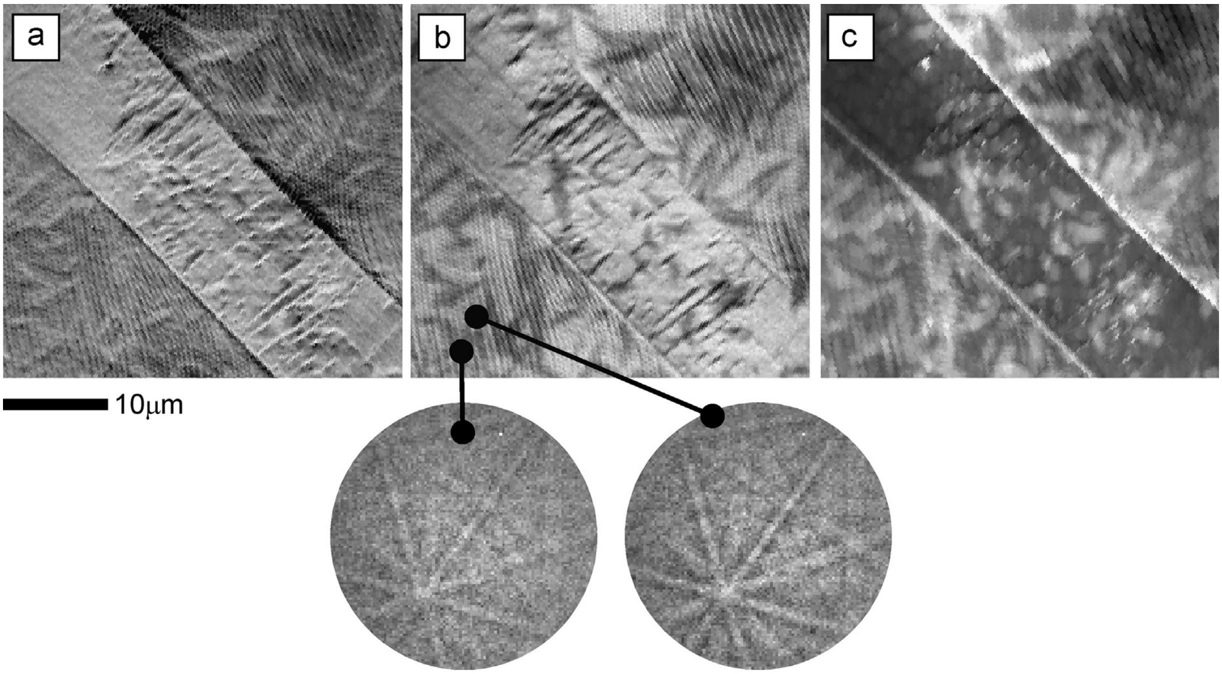

Fig. 21. (a) A VFSD I_{43} image, (b) IQ map and (c) a pattern difference map from a twin in a copper foil along with EBSD patterns from specific points in the OIM scan.

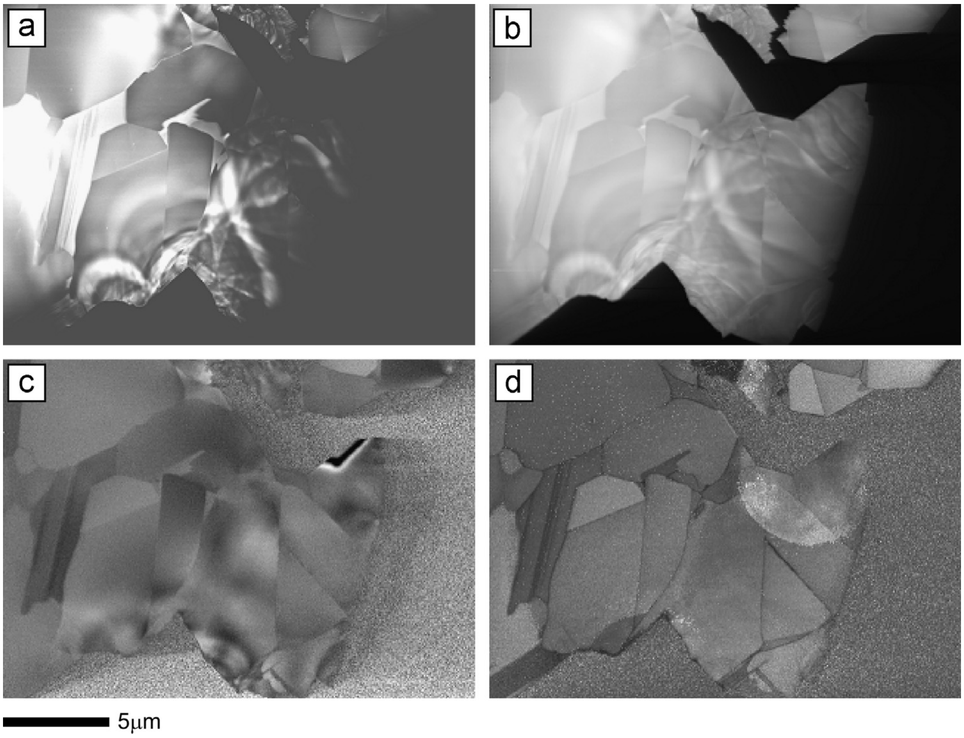

Fig. 22. Images from T-EBSD sample: (a) FSD image, (b) VFSD bottom image ($I_{52}+I_{53}+I_{54}$), (c) VFSD background corrected center ROI image (I_{33}), and (d) IQ map.

works equally well for the transmission and traditional EBSD geometries; however, the signals reaching the detector differs between the two geometries. In regular EBSD the signal is a mix of both the diffracted and scattered electrons. In transmission EBSD the contribution from the diffracted electrons dominates. In the T-EBSD, the VFSD image may be compared to a dark field STEM image which is a summation of the diffracted electrons through the entire probed thickness of the sample at any point. This may result in multiple superimposed grains being imaged. In a corresponding EBSD map only the orientation of the grain at the beam exiting side of the sample is measured because the EBSD pattern is dominated by contributions from the crystal lattice at the location of the exiting beam.

Fig. 22 compares FSD and VFSD images with an IQ map for a sample in the T-EBSD mode. The increased image resolution and strong diffraction contrast due to the strong diffracted signal at the FSD detector mounted at the bottom of the phosphor screen can be observed in Fig. 22(a). The corresponding VFSD image from the combined I_{52}, I_{53} and I_{54} bins shown in Fig. 22(b) shows similar contrast but is less sensitive to the specimen thickness allowing a larger area to be imaged successfully compared to the FSD image. Applying a background correction to the incoming patterns changes the contrast significantly as shown in Fig. 22(c).The diffraction details disappear and an orientation contrast image is generated such that the individual grains can be identified. An IQ map is shown in Fig. 22(d) for comparison.

Also, because of the thickness summation, the projection of the transmitted FSD signal on the phosphor screen changes with sample thickness. This may be visualized by comparing VFSD images from different locations along a vertical axis, for example I_{13} with I_{53}. Two “image planes” can be recognized in the images, a static plane that represents the lower surface of the specimen and a moving plane that represents the top surface of the sample. The amount of shift between these two superimposed images is caused by variations in specimen thickness.

7. Conclusions

The use of the EBSD detector as an imaging device allows for a great amount of flexibility in image formation. Through extreme binning of the EBSD CCD camera it is possible to collect images at a rate comparable to slow scan imaging in the SEM. VFSD data can also be collected concurrently with the usual orientation data during an EBSD scan. If patterns are recorded, VFSD images can be formed with even more flexibility during post-processing.

By forming composite images of the 25 simultaneously collected images it is possible to suppress or isolate the contrast of interest. Determining the best recipe for highlighting a particular microstructural feature is not always obvious and changes with different samples, SEM/EBSD geometry and SEM/EBSD operating conditions. Nonetheless, having the flexibility of utilizing 25 VFSD images provides a myriad of combinations for characterizing different aspects of microstructure.

It should be emphasized that the EBSD patterns need not be of sufficient quality for indexing. Images can be formed from surfaces too rough to produce index-able patterns. Thus, like SEI and BEI, the VFSD images provide only visualizations of the microstructure—they do not contain the quantitative data intrinsic to conventional OIM maps. However, VFSD images can be combined with conventional EBSD and XEDS mapping and correlative imaging between all of these techniques can be realized.

It is beyond the scope of this work to explore in detail all of the aspects of this imaging technique. We have begun investigating the potential of using VFSD in phase differentiation [11], automated directed scanning [18], and measuring crystallographic texture; however, these new areas are just being explored and we expect other application areas, more detailed analysis of the physical phenomena and more quantitative data processing approaches to emerge.

Acknowledgments

Scott Lindeman of EDAX is gratefully acknowledged for his efforts in implementing the necessary code to operate the camera at the very high binning conditions.

Very helpful discussions with Marc De Graef of Carnegie Mellon University, Gert Nolze of BAM Federal Institute for Materials Research and Testing and Eric Payton of Alfred University are acknowledged.

We are indebted to several people for access to samples and data. Thanks to Josh Kacher of Lawrence Berkeley National Laboratory for the Tungsten-Rhenium sample; Jan Honolka and Jaromír Kopeček of the Institute for Physics of the Academy of Sciences of the Czech Republic, Zheng Han, Sébastien Pairis, Vincent Bouchiat of the Institut NEEL CNRS/UJF and Felix Reinauer of EDAX Germany for providing data on the copper foil samples; Andrew Davis from the University of Chicago for the Zircon sample; and Klemens Kelm of DLR – Cologne for the T-EBSD sample.

References

[1] B.L. Adams, S.I. Wright, K. Kunze, Orientation imaging: the emergence of a new microscopy, Metall. Trans. A 24 (4) (1993) 819–831.

[2] A.P. Day, T.E. Quested, A comparison of grain imaging and measurement using horizontal orientation and colour orientation contrast imaging, electron backscatter pattern and optical methods, J. Microsc. 195 (3) (1999) 186–196.

[3] D.J. Prior, P.W. Trimby, U.D. Weber, D.J. Dingley, Orientation contrast imaging of microstructures rocks using forescatter detectors in the scanning electron-microscope, Mineral. Mag. 60 (1996) 859–869.

[4] Forward Scatter Detector, EDAX Product Bulletin, 2011.

[5] S.I. Wright, M.M. Nowell, EBSD image quality mapping, Microsc. Microanal. 12 (2006) 72–84.

[6] S.I. Wright and M.M. Nowell, Microstructure characterization using EBSD image quality mapping, in: Proceedings of the 13th Conference and Workshop on Electron Backscatter Diffraction (Unpublished work), Royal Microscopy Society, Oxford, 2006.

[7] E.J. Payton, G. Nolze, The backscatter electron signal as an additional tool for phase segmentation in electron backscatter diffraction, Microsc. Microanal. 19 (4) (2013) 929–941.

[8] R.A. Schwarzer, J. Sukkau, Electron back scattered diffraction: current state, prospects and comparison with x-ray diffraction texture measurement, Banaras Metall. 18 (2013) 1–11.

[9] M. De Graef, Forward modeling of electron signals for electron microscopy. in: Proceedings of the ICMR Summer School on Materials in 3D: Modeling and Imaging at Multiple Length Scales (Unpublished work), Santa Barbara, 2013.

[10] S. Wright, M. Nowell, High-speed EBSD, Adv. Mater. Process. 166 (2008) 29–31.

[11] M.M. Nowell, S.I. Wright, Phase differentiation via combined EBSD and XEDS, J. Microsc. 213 (2004) 296–305.

[12] S.I. Wright, M.M. Nowell, D.P. Field, A review of strain analysis using electron backscatter diffraction, Microsc. Microanal. 17 (2011) 316–329.

[13] D.J. Dingley, S.I. Wright, M.M. Nowell, Dynamic background correction of electron backscatter diffraction patterns, Microsc. Microanal. 11 (S02) (2005) S528–S529.

[14] P.W. Trimby, Y. Cao, Z. Chen, S. Han, K.J. Hemker, J. Lian, X. Liao, P. Rottmann, S. Samudrala, J. Sun, J.T. Wang, J. Wheeler, J.M. Cairney, Characterizing deformed ultrafine-grained and nanocrystalline materials using transmission Kikuchi diffraction in a scanning electron microscope, Acta Mater. 62 (2014) 69–80.

[15] R.R. Keller, R.H. Geiss, Transmission EBSD from 10 nm domains in a scanning electron microscope, J. Microsc. 245 (2011) 245–251.

[16] P.W. Trimby, Orientation mapping of nanostructured materials using transmission Kikuchi diffraction in the scanning electron microscope, Ultramicroscopy 120 (2012) 16–24.

[17] S. Suzuki, Features of transmission EBSD and its application, JOM 65 (9) (2013) 1254–1263.

[18] C.T. Wu, B.L. Adams, C.L. Bauer, D. Casasent, A. Morawiec, S. Ozdemira, A. Talukder, Mapping the mesoscale interface structure in polycrystalline materials, Ultramicroscopy 93 (2002) 99–109.